Journal of Superconductivity and Novel Magnetism (2019) 32:3295–3304
https://doi.org/10.1007/s10948-019-5093-5

ORIGINAL PAPER

Magnetic and Magnetotransport Characteristics of Cr-Substituted $Ni_{55}Mn_{34}Sn_{11}$ Thin Films Grown by Magnetron Sputtering

Barsha Borgohain[1,2] · P. K. Siwach[2] · Nidhi Singh[1,2] · K. V. R. Rao[3] · H. K. Singh[1,2]

Received: 12 December 2018 / Accepted: 27 March 2019 / Published online: 15 April 2019

Abstract
Highly oriented Cr-substituted $Ni_{55}Mn_{34}Sn_{11}$ Heusler thin films having thickness ~ 400 nm were deposited by Ultrahigh vacuum dc magnetron sputtering on MgO (100) substrates. At room temperature, the films exhibit a mixture of dominant $L2_1$ cubic austenite phase, as revealed by the intense (002) and (004) peaks, along with small fraction of the orthorhombic–martensitic phase. Surface morphology of the thin films showed distribution of Cr-rich and Cr-deficit regions together with patterned and aligned magnetic domains, thus bringing out the inherent room temperature ferromagnetism of the film. At temperatures above the Curie temperature, T_C ~ 321 K, the magnetic behaviour of the films is seen to follow the Curie law rather than the Curie–Weiss law. Ferromagnetic to antiferromagnetic transition appears at T_N ~ 247 K, which gives rise to exchange bias at low temperatures due to the coexistence of the two magnetic orders. This phase coexistence also leads to the formation of a spin glass state deep into the martensitic region. The film exhibits metal-like nature at high temperature and semiconductor-like behaviour with the lowering of temperature. A reentrant metallic state is observed at $T \leq 38$ K during cooling that persists up to ≤ 62 K in warming cycle. The hysteresis in the ρ–T curve spread over a very wide temperature range confirms the magnetic phase coexistence in the martensitic state in the present thin films. The magnetoresistance (MR) first increases (2.4% at 300 K and H = 50 kOe) with temperature and maximizes to around ~ 3.25% at T = 150 K and then starts decreasing. Its value in the glassy state is very small. This shows that a magnetic liquid like state is more conducive to larger MR.

Keywords Sputtering · Heusler alloys · Thin films · Austenite–martensite transformation

1 Introduction

In recent times, off-stoichiometric Ni–Mn–Sn Heusler compounds exhibiting martensitic transformation (MT) have drawn immense research interest due to their intrinsic multifunctional properties like magnetoresistance (MR), magnetic shape memory effect (MSME), magnetocaloric effect (MCE), exchange bias (EB), and spin glass (SG) behaviour [1–7]. Ever since Sutou et al. [8] first reported MT, this family of compounds has been centre of extensive investigations as their functional properties offer great potential for applications in diverse areas like spintronics, magnetic refrigeration technology, and magnetic actuation [5–7, 9, 10]. These compounds exhibit austenite phase (AP) with cubic $L2_1$ structure at high temperature which transforms to a modulated orthogonal or tetragonal martensite phase (MP) with the lowering of temperature. The austenite phase may be a pure paramagnetic (PM) phase or it can show a mixed paramagnetic–ferromagnetic (PM–FM) phase around the Curie temperature T_C. In contrast, the modulated martensite phase in general has coexistence of ferromagnetism and antiferromagnetism (AFM) and hence the formation of a spin glass state with the glass transition depending on the chemical composition [1–7, 11, 12].

In Ni–Mn–Sn full Heusler systems, the excess Mn atoms occupy the Ni or Sn sites and the hybridization between the Ni atoms and the Mn atoms on the Sn sites is an important driving force for the occurrence of MT [13, 14]. A first-order magnetocoupled structural phase transition in these compounds

✉ Nidhi Singh
singhnidhi@nplindia.org

✉ H. K. Singh
hks65.npl@nic.in

[1] Academy of Scientific and Innovative Research (AcSIR), Ghaziabad 228001, India

[2] CSIR-National Physical Laboratory, Dr. K. S. Krishnan Raod, New Delhi 110012, India

[3] Department of Physics, University of Rajasthan, Jaipur 302004, India

arises due to the strong coupling between the structural and magnetic transitions. The functional properties of Ni–Mn–Sn compounds can be tuned by varying the elemental composition as the structural and magnetic phase transitions in these systems are strongly dependent on the e/a ratio (number of valence electrons per atom in the unit cell) [15]. It has been reported that the martensitic transition temperature (T_M) increases (decreases) with the increase (decrease) of the e/a ratio. Xuan et al. studied various multifunctional properties of $Mn_{50}Ni_{40}Sn_{10}$ bulk alloys and found a maximum EB field of 910 Oe [16]. Chatterjee et al. observed a reentrant spin glass state at low temperature in $Ni_2Mn_{1.36}Sn_{0.64}$ alloy [12]. Santos et al. found a highly ordered growth of columnar microcrystalline grains in $Ni_{50}Mn_{37}Sn_{13}$ ribbons having cubic $L2_1$ austenite phase at room temperature [17]. Zhang et al. studied the effect of annealing on the magnetocaloric properties of Mn-rich $Ni_{43}Mn_{46}Sn_{11}$ ribbons and reported a large magnetic entropy change (ΔS_M) of 43.2 J/kg K in a field change of 5 T [18]. There are many studies on Ni–Mn–Sn Heusler alloys in their bulk and ribbon forms [8, 10–12, 16–19]. However, for applications in the emerging nano- and microelectronic technologies such as magnetic actuators, magnetic refrigeration, and magnetic shape memory devices, it is important to study the properties of Ni–Mn–Sn compounds in thin film form. Studies have shown that the microstructure and martensitic transition behaviour changes significantly in thin films [20]. Besides the innate stress involved during MT, in thin films, there is the added strain due to lattice mismatch between the substrate and the material to be deposited. These effects substantially influence the MT behaviour, and a broader transition as well as a change in the corresponding transformation temperatures have been reported [21–23]. Substrate constraints, confinement of the nucleus, and size scale effects on the mean free path of transition dislocations are some of the reasons behind observed transformational changes in thin films [22, 23].

Vishnoi et al. while investigating polycrystalline Ni–Mn–Sn films on Si substrates in the thickness range from 120 nm up to 2.5 μm found a suppression of the MT below 410 nm and an increase in the MT temperature with increasing film thickness up to 1400 nm, above which there is a degradation in the phase transformation due to the presence of disorder [24]. In another study, Auge et al. showed that ultrathin (~ 10 nm thick) films of Ni–Mn–Sn films showed martensitic transformations but with a broader transformation range than the bulk counterparts and also reported that close to the interfaces of the substrate, the aforementioned transformation was considerably suppressed [20]. Dubowik et al. reported a maximum negative MR of ~ 22% at 110 K over the martensitic transformation in epitaxial $Ni_{50}Mn_{35}Sn_{15}$ thin films grown on MgO substrates [25]. Behler et al. reported the presence of thickness dependent exchange bias in the martensite state in Ni–Mn–Sn (~ $Ni_{50.000}Mn_{34.375}Sn_{15.625}$) epitaxial thin films and emphasized upon the fact that a martensitic transition in Ni–Mn–Sn thin films is a necessary condition for exchange bias [26]. Compositional variation or substitution by fourth element has been observed to bring about a change in the austenite–martensitic (AM) transition behaviour as well as in the magnetic properties of Ni–Mn–Sn Heusler compounds in the bulk and ribbon forms [27–32]. The phase transformation and magnetic properties in Heusler thin films are strongly dependent upon on the various deposition parameters such as composition, substrate temperature, gas pressure, and target to substrate distance [24]. Machavarapu et al. reported a relatively large exchange bias field of 139 Oe at 5 K in Ni–Co–Mn–Sn thin films compared to the reported exchange bias field of 41 Oe at 2 K in Ni–Mn–Sn films [33, 34]. 'Co' substitution in Ni–Mn–Sn films was studied by Modak et al., and they reported more than 3.8-fold increase in the magnetic entropy change and 8.9-fold increase in refrigeration capacity and shift of T_C towards higher temperature due to Co substitution [35]. Golub et al. studied the magnetic properties of $Ni_{46}Mn_{36.8}Sn_{11.4}Co_{5.8}$ epitaxial film by ferromagnetic resonance to understand the magnetic interactions of the twinned martensite phase [36].

The properties of full Heusler Ni–Mn–Sn compounds are extremely sensitive to the compositional variation. Although the austenite phase of Ni–Mn–Sn full Heuslers exhibits $L2_1$ structure, but the structure of the martensitic phase is dependent on the Sn concentration. Krenke et al. [37] showed that in $Ni_{50}Mn_{50-x}Sn_x$ (x varies from 5 to 25) bulk alloys, the martensitic phase structure varies as 10M, 14M, or L10 with the increase of Sn concentration. They emphasized on the presence of FM interactions in the M-phase for the occurrence of the MSME for the alloys with $x = 13$ and 15. They also derived the e/a dependence of the MT, and reported that for e/a > 8.1, the $Ni_{50}Mn_{50-x}Sn_x$ system is in the martensitic state at room temperature. The Curie temperature of both the A-phase and M-phase decreases with the increase of the e/a value; however, the decrease of the T_{CM} of the M-phase is more rapid than that of the T_{CA} of the austenite phase and T_{CM} is expected to disappear for e/a = 8.2, i.e. $x = 10$ [37]. Tao et al. [38] studied the $Ni_{50-x}Mn_{41+x}Sn_9$ ($x = 0$–19) alloys from Ni-rich to Mn-rich composition. They observed the occurrence of MT only in the Mn-rich alloys with $11 \le x \le 17$ and no γ phase till $x = 17$. The magnetization change across MT was largest for the composition $Ni_{37}Mn_{54}Sn_9$ (ΔM = 44 Am^2/kg). Aydogdu et al. [39] investigated the compositional variation of Sn content on the magnetostructural behaviour of $Ni_{50}Mn_{40-x}Sn_{10+x}$ ($x = 0, 1, 2, 3$) alloys and found that the MT temperature as well as saturation magnetization decreases with the increase of Sn content. Sokolovskiy et al. [40] investigated the influence of chemical and structural disorder in Ni-rich Ni–Mn–Sn alloys using ab initio calculations and was able to explain the observed variation of the Curie temperature of the FM region by intermixing of the Mn and Sn in their sublattices. Recently, Kundu and Ghosh [41] have

reported the effect of different parameters like site occupancy, composition, and magnetic structure on the martensitic transition of $Mn_2Ni_{1+x}Sn_{1-x}$ alloys where they showed the crucial role of the 4d site occupancies in the inverse Heusler systems. FM interactions between Mn at (¼,¼,¼) sites and Mn at the Sn sites stabilize the austenite phase. However, due to the decrease of the interatomic distances under structural distortion of the MT, there arise AFM exchange interactions between them that strengthen the competing Jahn–Teller effect and result in stabilizing the martensite phase. The Ni atoms at the Sn site weaken the covalent bonding between the Mn, Ni, and Sn atoms in their original sites and thus aid in the destabilization of the austenite phase. This study brings forth the delicate balance of Ni and Mn atoms at the 4d sites (i.e. the Sn sites) or in the other words the importance of the Ni–Mn hybridisation in the stability of the martensite phase. This study was able to explain to an extent the discrepancies between the experimental observations that reported the stability of the austenite phase down to very low temperature and the earlier DFT calculations which predicted a stable martensite phase at low temperatures in Mn-rich Ni–Mn–Sn systems [41].

Very limited studies are available on the Cr substitution at Ni/Mn sites in the Ni–Mn–Sn/Mn–Ni–Sn compounds. Pandey et al. [27, 28] observed a large inverse magnetocaloric effect (~ 35 J/kg K) and giant magnetoresistance (~ 67%) in $Ni_{45}Mn_{43}CrSn_{11}$ bulk alloys along with a shift of 30 K in the MT temperature with the application of hydrostatic pressure of 0.95 GPa. Czaja et al. [42] studied the effect of Cr substitution on the magnetocaloric effect in Ni–Mn–Sn alloys and found that though higher amount of 'Cr' gives a broader temperature window for the magnetic entropy change; the refrigerant capacity is much smaller than the alloy with lower Cr concentration. Recently, we have also observed an enhancement in the ferromagnetism in Cr-substituted $Mn_{48+x}Cr_{3-x}Ni_{39}Sn_{11}$ ($x = 0, 1$) ribbons and brought forth the crucial role played by the amount of Cr substitution and critical Mn/Cr ratio which overall affected the magnetic and electrical transport properties in these alloys [43]. Despite these studies on bulk compounds, there is hardly any study on the Cr substitution at Ni/Mn sites in Ni–Mn–Sn thin films. Since the clamping effect of the substrate and the associated degree of strain provide additional degree of freedom to tune the magnetic and transport properties, therefore thin films naturally attain added importance. In view of this, we have attempted to optimize the conditions for the growth of Cr substituted Ni–Mn–Sn thin films on MgO (100) substrates (lattice parameter 4.216 Å). In the present work, we report our studies on the growth of Cr-substituted Ni–Mn–Sn thin films on (100)-oriented MgO substrate and its structural, magnetic, and magnetotransport properties. To reduce the substrate-induced strain, MgO (100) substrate which has low lattice mismatch with Ni–Mn–Sn system was chosen with the growth relationship between the film and the substrate that is film (110)//MgO (100).

2 Experimental

High-quality Ni–Mn–Cr–Sn thin films (thicknesses ~ 400 nm) were deposited on the single crystal MgO (100) substrates from commercial ~ 2-in.-diameter target by ultrahigh vacuum (UHV) dc magnetron sputtering having load lock facility (The UHV chamber is made in India and assembled with magnetic guns from Angstrom Sciences, Turbo-molecular pump from Pfeiffer and DC power supply from MAG Puls.). Before deposition of the films, the deposition chamber was cleaned by attaining a vacuum of up to $\sim 10^{-9}$ mbar and then flushed twice by 6 N pure Ar. Prior to deposition, the MgO substrates were cut in size of 3×5 mm^2 and ultrasonically cleaned in acetone, isopropyl alcohol, and finally in doubled distilled water couple of times to remove any surface contamination. As the traces of impurities, particularly oxygen is detrimental to the structure and magnetoelectrical properties of Ni–Mn–Cr–Sn thin films so the MgO substrates were first placed in load lock chamber at ~ 200 °C for 6 h at a base vacuum of ~ 5×10^{-6} mbar. After that, the MgO substrates were transferred to the deposition chamber (base vacuum of ~ 5×10^{-9} mbar) and left for a couple of hours. The substrates were heated from room temperature to 500 °C in 1 h and kept at 500 °C for 2 h to prepare the surface for growth of Ni–Mn–Cr–Sn thin films.

To obtain the optimum deposition condition, we tried many rounds of thin film deposition by varying the deposition temperature and gas pressure. For a low gas pressure of ~ 7×10^{-3} mbar, the optimum temperature was found to be 800 °C for obtaining a good crystalline Ni–Mn–Cr–Sn film. So the Ni–Mn–Cr–Sn thin films were deposited on MgO substrate at 40 W dc power at a dynamic 6 N pure Argon gas pressure of ~ 7×10^{-3} mbar at ~ 20 sccm flow rate. To have uniform deposition, the substrate holder was rotated at 10 rpm. After deposition, the films were kept at 800 °C for 1 h and were then transferred to load lock chamber and kept there for couple of hours before taking them out for further characterization. The thickness was calculated by making steps and measuring step height through AFM' (Atomic Force Microscopy) and stylus profilometer. The as-synthesized Ni–Mn–Cr–Sn thin films were subjected to structural and microstructural characterization through high-resolution X-ray diffraction, field electron scanning electron microscopy, energy-dispersive X-ray spectroscopy (EDS), and atomic/magnetic force microscopy. Magnetic characterization was done by SQUID magnetometer (MPME-XL, Quantum Design), and magnetotransport was measured by a physical property measurement system (PPMS, Cryogenics).

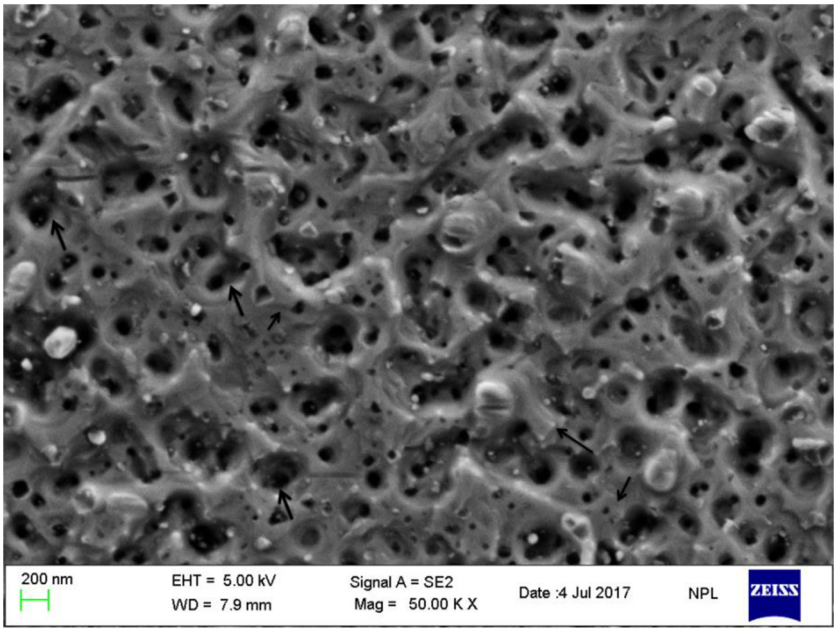

Fig. 1 FESEM picture showing the surface morphology of Ni–Mn–Cr–Sn thin film. The thin arrows mark the dominant layered type surface having average composition $Ni_{51}Mn_{33}Cr_5Sn_{11}$. The thick arrows mark the pit like features which have chemical composition of $Ni_{50}Mn_{32}Cr_7Sn_{11}$ and interrupt the continuous layer growth

3 Results and Discussion

In the present case, the film thickness is found to be ~ 400 nm. EDS measurements on the Ni–Mn–Cr–Sn films show that all the films have nearly even distribution of Cr-rich and Cr-deficient regions. A typical FESEM (field emission scanning electron microscope) micrograph depicting the representative surface morphology of the film is shown in Fig. 1. The film surface consists of the continuous surface having layered growth, which is frequently interrupted by surface pits. The EDS of the pits appearing in the surface reveals an average composition of $Ni_{50}Mn_{32}Cr_7Sn_{11}$. In contrast, the rest of the film has an average composition $Ni_{51}Mn_{33}Cr_5Sn_{11}$. This clearly outlines the fact that there is only slight variation in the chemical composition of the pits and the rest of the film and keeping in view the accuracy of EDS the film can be regarded as chemically homogeneous. However, Sn has better chemical homogeneity as compared to the rest of the constituents.

It must be pointed out here that the substitution of Mn ions at Sn sites enhances AFM order due to the reduced Mn–Mn distances along the [110] direction and result in a noncollinear spin structures, which in turn can pin the FM domains in different configurations and hence give rise to the difference between the magnetizations measured under different protocols [37]. In view of this, the chemical inhomogeneity observed in the present case may not have any drastic bearing on the magnetic properties of the films.

The structural aspects of the film are elucidated by the high-resolution X-ray diffraction (HRXRD) measurements as shown in Fig. 2. The film shows very intense peaks corresponding to the (002) and (004) planes of the $L2_1$ cubic phase. Absence of any other peak belonging to the cubic phase confirms a highly textured growth in [001] direction. The films grow with the planar relation MgO (100)|| Ni–Mn–Cr–Sn (110). Thus, the (hh0) planes of the film are parallel to the (h 0 0) plane of MgO. Three other peaks which belong to the orthorhombic phase, with much smaller intensity than the (00 *l*) reflections of the $L2_1$ phase, are also seen. The presence of these small peaks shows that the martensitic phase could be present in small quantity even at room temperature. The pseudo-Voigt approximation for fitting the diffraction peaks yields the half width at full maximum (FWHM) of the (002) and (004) $L2_1$ reflections as 0.689° ± 0.007° and 0.777° ± 0.015°, respectively. In the inset is shown the rocking curve of the (004) diffraction peak of the $L2_1$ phase. Employing the

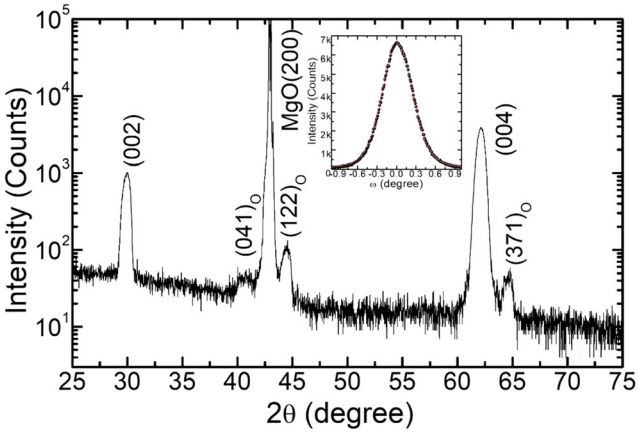

Fig. 2 The HRXRD $\omega/2\theta$ scan of the Ni–Mn–Cr–Sn film on MgO (001) substrate. The peaks marked by the subscript 'o' represent to the orthorhombic phase while the (002) and (004) peaks belong to the L21 cubic phase. The inset shows the rocking curve of the (004) peak

pseudo-Voigt approximation for fitting, the FWHM of this rocking curve is found to be 0.559° ± 0.001°. The FWHM values corresponding to the rocking curve show the good crystalline quality of the thin film. The out-of-plane lattice constant is determined from the HRXRD spectrum of Fig. 2 using the Bragg equation. The lattice constant of the film is found to be 5.9691 Å ± 0.0012 Å. These values are slightly smaller than the one obtained for bulk $Ni_{50}Mn_{35}Sn_{15}$ (5.995 Å) [37]. The slightly lower value of the unit cell parameter could possibly be due to substrate-induced effects like local epitaxial growth and substrate-induced stress.

Further topographical analysis is done by AFM' (atomic force microscopy) and MFM (magnetic force microscopy) measurements (Fig. 3). As seen in Fig. 3 (main frame), the topography of the film has average surface roughness ~ 40 nm, which is about ~ 10% of the thickness of the film. As pointed out in discussion of the FESEM results, one major source contributing to the roughness is the formation of pits in the film surface (the darker regions in Figs. 1 and 3), which has slight deviation in the chemical composition also. The inset of Fig. 3 shows the MFM image of the film surface. The MFM clearly shows very ordered magnetic domain structure, as evidenced by the presence of well aligned domain stripes (marked by arrow). The centres of the two successive stripes are separated by ~ 1.8 μm. The comparison of the FESEM and AFM' topographs as well as the magnetic structure in the MFM image demonstrates that formation of pits is barely able to affect the magnetic order in the film, which remains in a well-ordered FM state at room temperature. The absence of any sharp contrast in the regular surface and the pits in the MFM image also suggests that they possess nearly similar magnetic behaviour, e.g. nearly identical FM Curie temperature.

Detailed magnetic characterization was done by temperature and magnetic field–dependent magnetization (M-T and M-H) measurements. During the M-T measurements, the magnetic field (H = 100 Oe) was applied parallel to the film surface along the longer dimension of the film. The M-T measured under ZFC (zero-field cooled) and FCW (field cooled warming) protocols is plotted in Fig. 4. The ferromagnetic transition temperature (Curie temperature T_C) was determined from the H/M-T plot shown in the inset of Fig. 4. In the temperature range 355 K < T < 400 K, H/M follows the Curie law ($\chi \sim \frac{C}{T}$) (the blue line shows the Curie law fit to the experimental data), and in a shorter temperature range 322 K < T < 340 K, it obeys the Curie–Weiss law ($\chi = \frac{C_W}{T - T_c}$) (the navy blue curve). This anomalous magnetization behaviour, viz., deviation from the Curie–Weiss law in the higher temperature regime is really intriguing and could be due to the complex interplay between the sublattice magnetic orderings.

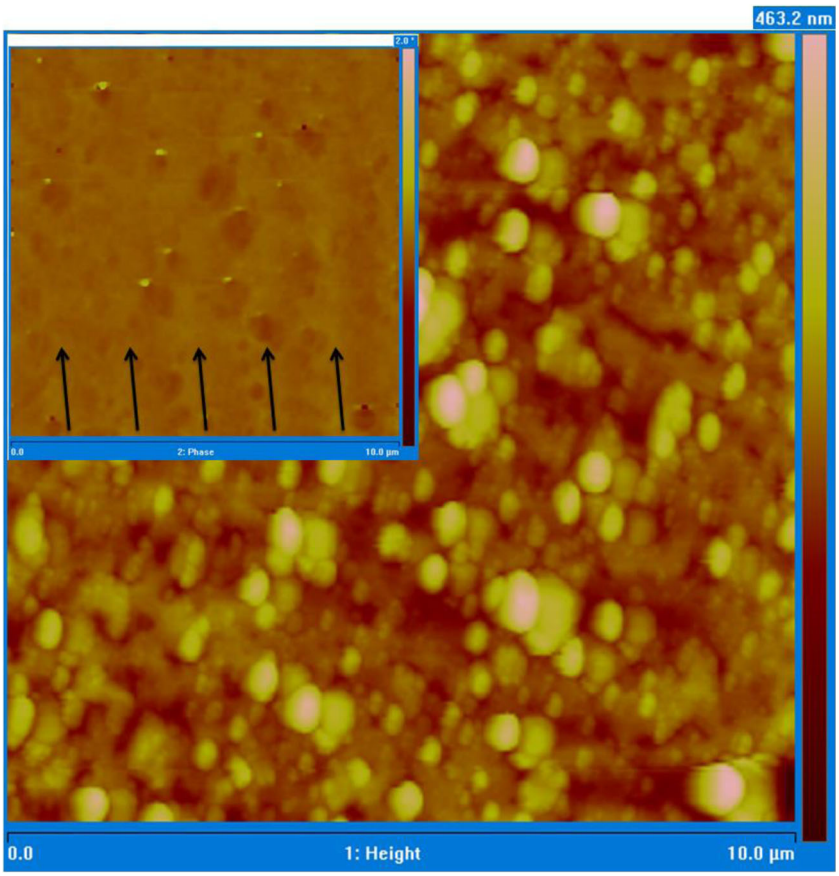

Fig. 3 (Main frame) AFM' image showing the topography of the Ni–Mn–Cr–Sn film on MgO (001) substrate. (Inset) The MFM image portraying the magnetic ordering in these films. Near identical colour contrast between the regular surface and pits therein is suggestive of nearly similar FM characteristics of the two regions

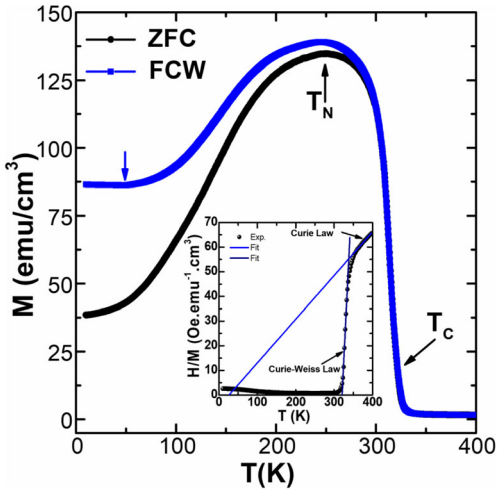

Fig. 4 (Main frame) ZFC and FCW magnetization measured at H = 100 Oe. The inset shows the Curie and Curie–Weiss law fits to the H/M-T data. For details see the text

The Curie temperature obtained from the best Curie–Weiss fit ($R^2 = 0.996$) is $T_C = 321$ K. The PM–FM transition is quite sharp and magnetic moment peaks around $T \sim 247$ K and then starts decreasing, first slowly, and then rapidly at $T < 200$ K. The decrease in magnetization is due to the onset of the AFM ordering around the peak, which corresponds to the Neel temperature $T_N \sim 247$ K. In the lower temperature region, the magnetization (at 10 K of ≈ 38 and ≈ 86 emu/cm^3, respectively) for the ZFC and FCW curves clearly pronounces the existence of a mixed state comprising of FM and AFM orders. The mixed state has a weak reentrant FM order as shown by slight increase in the FCW magnetization below 50 K (marked by blue arrow). Another interesting feature is the divergence of ZFC and FCW M-T curves which appears at $T \sim 290$ K but becomes prominent in the lower temperature region, where the AFM–FM coexistence dominates. This is clearly suggestive of the existence of a glassy state.

To extract more information regarding the magnetic ordering in the different temperature regimes, we measured the magnetic field–dependent magnetization (M-H) at several temperatures at $T < T_C$. Some of the representative M-H curves taken at different temperatures are shown in Fig. 5. None of the M-H loops exhibit any saturation up to 600 Oe, but the maximum moment is observed just above T_N. It is observed that the M-H loop at 10 K narrows down at low fields and then slightly widens and closes. Such behaviour is due to the presence of much larger AFM fraction than FM fraction. Consequently, the EB is considerably lowered.

The different parameters of the M-H loops have been extracted and analysed in detail. The remanent magnetization ($M_r = \frac{M_{r1} - M_{r2}}{2}$, where M_{r1} and M_{r2} are the positive and negative remanence respectively) is plotted in Fig. 6. As the temperature is lowered below T_C, the M-H loops open up. M_r peaks around 200 K − 150 K, i.e. at temperatures much below T_N.

The coercivity ($H_C = \frac{H_{c1} - H_{c2}}{2}$, where H_{C1} and H_{C2} are the positive and negative cycle coercivity) is seen to increase till about $T \sim 50$ K and then decreases. The variation of the positive and negative coercivity (H_{C1} and H_{C2}) and the coercivity (H_C) is plotted in Fig. 7. From Fig. 7a, it is clear that on lowering the temperature, both scale linearly but asymmetrically till $T \sim 50$ K and then the both turn negative in the lower temperature region. The asymmetry in the values of H_{C1} and H_{C2} and their negative values at $T = 10$ K clearly shows the presence of exchange bias (EB) effect in the film. The EB is prevalent throughout the temperature region $T < T_C$ but is more pronounced at lower temperatures. This clearly confirms the presence of AFM clusters at all $T < T_C$. This agree well with the structural data as unravelled by the XRD. Fig 7b shows the temperature dependence of the coercivity $H_C = \frac{H_{c1} - H_{c2}}{2}$ and a linear fit to the experimental data. The best linear fit of the type $H_C = H_0 + H_{CT}T$ yields $H_0 = 153 \pm 6$ Oe and temperature coefficient $H_{CT} = -0.47 \pm 0.03$ Oe/K.

Exchange bias is a characteristic of heterostructures/heterointerfaces (either artificial or natural) comprising of AFM and FM faces, wherein the exchange coupling between them produces a stable FM behaviour with high degree of anisotropy which may be unidirectional or uniaxial. In EB systems, the hysteresis loop associated with the FM/AFM heterostructure is generally centred about a nonzero magnetic field. The shift in H_C is attributed to large anisotropy associated with AFM and a weaker exchange energy coupling between the FM and AFM, and its magnitude is equal to the effective field associated with the interlayer exchange. The EB field defined as $H_{EB} = \frac{H_{C1} + H_{C2}}{2}$ is given in terms of the saturation magnetization (M_S), the thickness (d_F) of the FM, and J the interlayer exchange constant by [44]

$$H_{EB} = \frac{H_{C1} + H_{C2}}{2} = -\frac{J}{M_S d_F}.$$

As seen in the M-H loops, the M_S decreases with the lowering of the temperature and hence higher value of H_{EB}. The temperature dependence of the EB field is plotted in Fig. 8. The magnitude of the EB field is the highest at $T << T_N$ and its decreases sharply as the temperature approaches ~ 100 K. In general, the EB and the associated field are known to decrease with the increase in temperature; however, in case of Heusler alloys, it is not well investigated and understood. In view of the above expression, it appears that one of the factors responsible for decrease in the H_{EB} is due to the decrease in the AFM phase fraction contribution to the FM/AFM interfaces. This leads to (i) the weakening of the exchange coupling between the FM and AFM phases [44], (ii) increase in the M_S (as indicated by the M-H loops in Fig. 5), and (iii) increase in

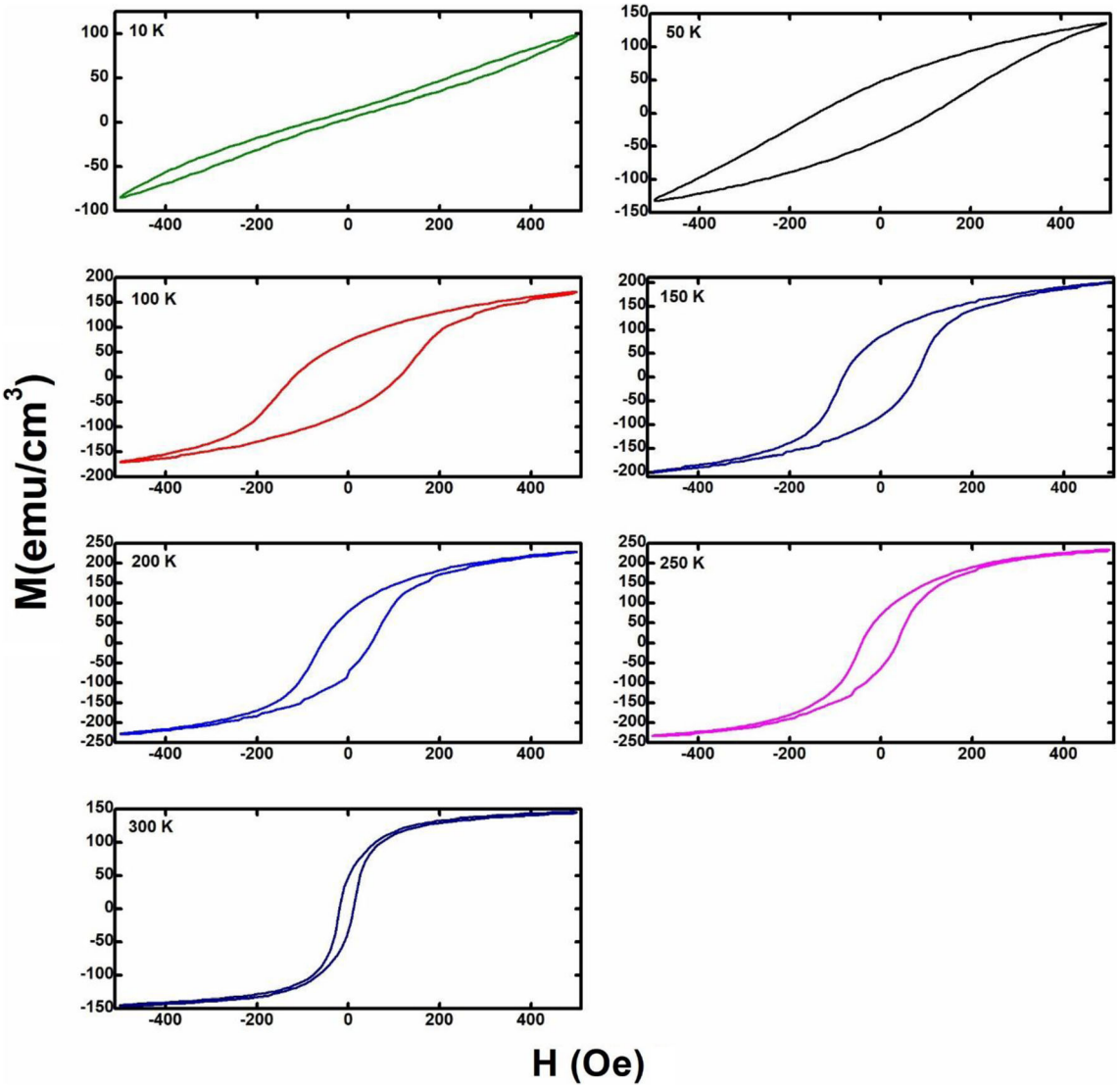

Fig. 5 Magnetic field–dependent magnetization (M-H) measured at different temperatures. For details of analysis, see the text

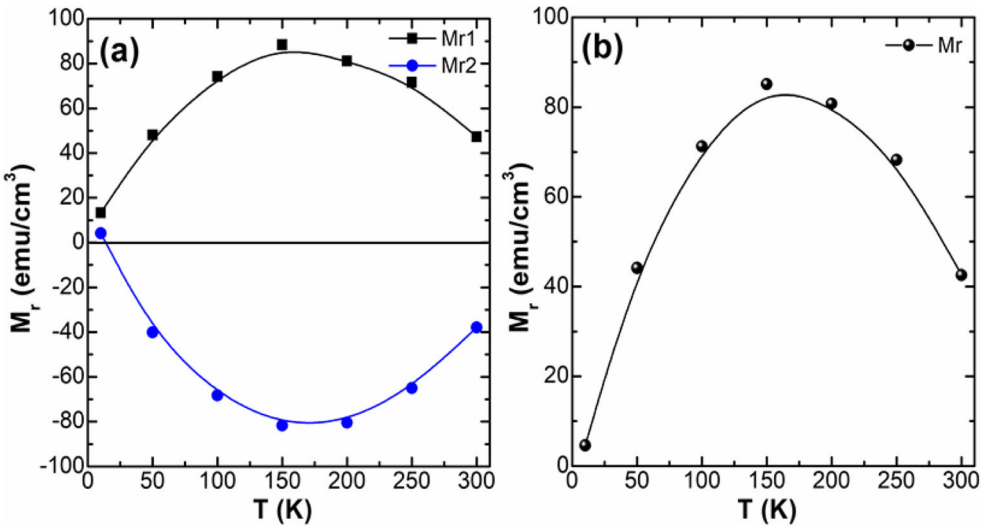

Fig. 6 **a** Temperature dependence of positive and negative remanence and **b** temperature-dependent average remanence

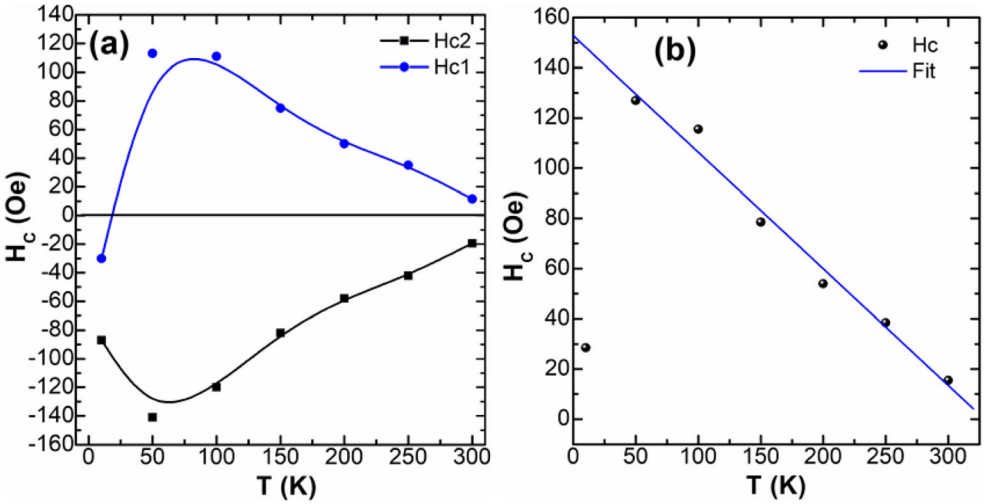

Fig. 7 **a** Temperature dependence of the positive and negative coercivity, H_{C1} and H_{C2}, and **b** temperature dependence of H_C and a linear fit to it using eq. $H_C = H_0 + H_{CT}T$

the thickness of the FM layers. All these factors lead to decrease in H_{EB}. Although, not exactly similar, but our results closely resemble that of Nayak et al. in case of bulk Mn_2PtIn [45].

The H_{EB}–T data has been fitted with empirical relation $H_{EB} = H_{EB0} + \zeta e^{\beta T}$. H_{EB0} is the EB field at temperature approaching infinity (high temperature); the coefficient ζ could be related to the exchange coupling. The best fitting ($R^2 = 0.99964$) parameters are found to be $H_{EB0} = -3.68 \pm 0.18$ Oe, $\zeta = -83.43 \pm 1.05$ Oe, and $\beta = -0.042 \pm 0.001$. Here we would like to point out that the origin of EB effect is also attributed to the glassy state [46], which is also an outcome of the FM and AFM interaction.

We have carried electrical transport studies to figure out the consequences of the changes in the magnetic phase profile on the charge transport and hence the nature of conduction in the film. We have also measured the isothermal magnetoresistance at several temperatures throughout the temperature range. The temperature-dependent resistivity (ρ–T) measured during cooling and warming is plotted in Fig. 9. The ρ–T follows metallic temperature dependence between 350 K and 240 K, and then it reverses the trend and shows a semiconductor like behaviour as T is lowered below $T_{AMs} \approx 219$ K. A peak is seen in the ρ–T curve at $T_{AMf} \approx 40$ K, which is followed by a reentrant weak metallic behaviour at $T < 36$ K. In the beginning of the warming cycle, the resistivity rises reversibly and peaks at $T_{MAs} \approx 62$ K. As the temperature is raised further up the resistivity shows a semiconductor like behaviour and changes slope at $T_{MAf} \approx 248$ K. At $T > T_{MAf}$, the ρ–T curve remains metallic up to 350 K. Here the temperature $T_{AMs} \approx 219$ K marks the beginning of the martensitic transition which finishes at $T_{AMf} \approx 40$ K in the cooling cycle.

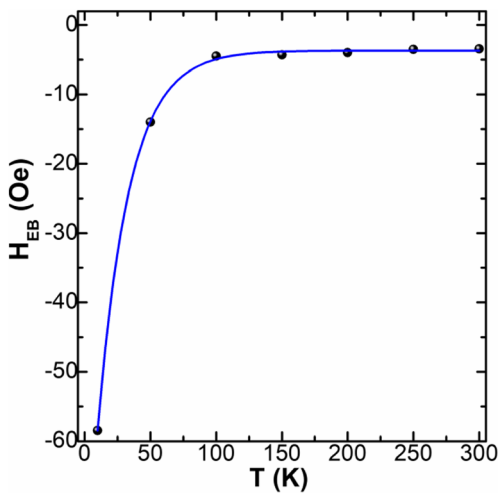

Fig. 8 Temperature dependence of the exchange bias field (H_{EB}). The experimental data is best fitted (blue solid line) by an empirical expression of the type $H_{EB} = H_{EB0} + \zeta e^{\beta T}$

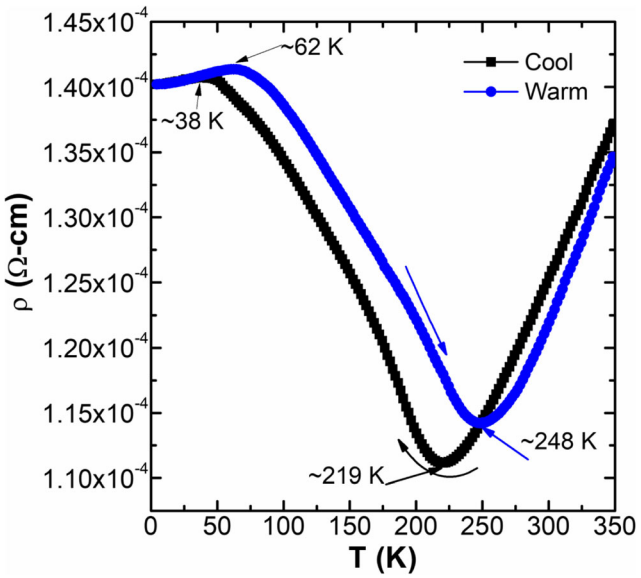

Fig. 9 Temperature dependence of resistivity measured during the cooling and warming cycle. Various transitions as discussed in the text are marked by arrow

Clearly, the reverse martensite to austenite transition begins at $T_{MAs} \approx 62$ K and finishes at $T_{MAf} \approx 248$ K. The reentrant metallic behaviour in the lower temperature regime is possible due to reentrant FM order. The hysteretic region in the ρ–T curve marks the regions which are dominated by the martensitic phase which appears to have a mixed magnetic profile with coexisting AFM and FM clusters.

The magnetic field dependence of resistivity (ρ–H) was measured at several temperatures in the temperature range 10 K $\leq T \leq$ 300 K, and some representative normalized ρ–H plots are shown in Fig. 10. The normalized resistivity ($\frac{\rho(H)}{\rho(H=0)}$) has been plotted to highlight the comparative behaviour. At 300 K, where the electronic phase is by dominated austenite-FM with small fraction of the martensite phase (as evidenced by the XRD but not reflected in the M-T and ρ–T measurements), the resistivity shows a linear ρ~H dependence without any hysteresis between the field increasing/decreasing cycles. The maximum magnetoresistance is MR ~ 2.46% at H = 50 kOe. At 240 K, the ρ–H behaviour becomes hysteretic and MR slightly increases to ~ 2.59%. The ρ–H hysteresis widens with a concomitant increase in the MR as the temperature is lowered further and at 150 K MR ~ 3.25%. As the temperature is lowered further down, the ρ–H hysteresis squeezes considerably and the MR decreases. For example, at T = 50 K and 10 K, the hysteresis gets successively narrower and MR ~ 1.54% and 1.14%, respectively. The ρ–H measurements show that MR peaks in the regions just below the T_N, that is, in the region where the FM and AFM phases coexist most delicately. While in the glassy regime, the MR is the lowest. Thus, the ρ–H data brings out that a magnetic liquid like state is conducive to the higher MR. Here we would like to mention that the magnitude of the MR is lower than reported values in case of Ni–Mn–Sn bulk samples of nearly similar composition [47] and but higher than other Heusler alloys like Fe_2CoSi [48]. In fact MR, though small in the present, thin films is comparable to the values obtained in case of the best of epitaxial thin films of Heusler alloys [49].

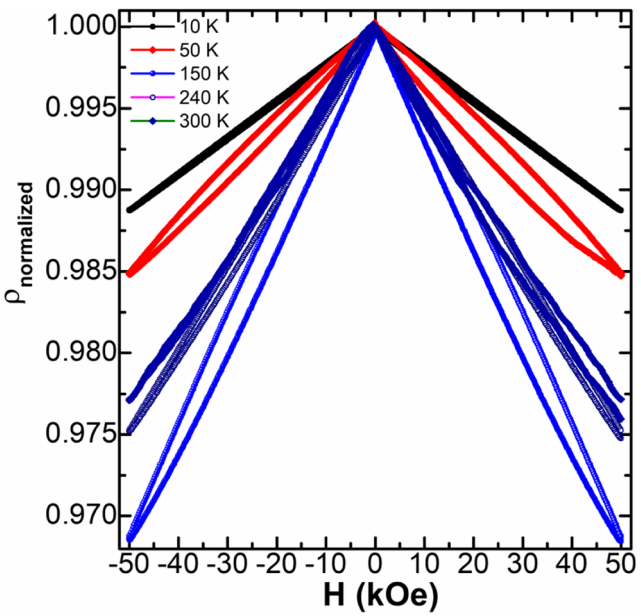

Fig. 10 Magnetic field (H) dependence of resistivity measured during warming cycle at several temperatures (isothermal magnetoresistance). Here for the sake of clarity in comparison the normalized resistivity is given by $\rho_{normalized} = \frac{\rho_{(H=0)}}{\rho_{(H)}}$ has been plotted

4 Conclusions

The structural, magnetic, and electrical properties of Cr-substituted $Ni_{55}Mn_{34}Sn_{11}$ Heusler thin films having thickness ~ 400 nm were studied. These films were grown on MgO (100) single crystal substrates by dc magnetron sputtering in an UHV chamber having load lock facility. The films showed Cr-rich and Cr-deficit regions dispersed all over the surface. Intense peaks corresponding to (002) and (004) planes of the $L2_1$ cubic phase confirm highly oriented growth in the [001] direction. However, some small intensity peaks corresponding to the orthorhombic phase signature the presence of a small fraction of the martensitic phase even at room temperature. The calculated out-of-plane lattice parameter is ~ 5.9691 Å ± 0.0012 Å. Room temperature MFM studies reveal the presence of aligned stripped magnetic domains in the films and brings out their FM character. The Curie temperature of the austenite phase is observed at T_C ~ 321 K and in the higher temperature regime, i.e. for T > 350 K, the magnetic nature of the films deviate from the Curie–Weiss behaviour. Divergence of the ZFC/FCW curves and the decrease of magnetization at T < 290 K together with the presence of remanent magnetization at low temperatures suggest the coexistence of antiferromagnetic/ferromagnetic phases and spin glass state. The presence of exchange bias behaviour in the lower temperature region is confirmed by the asymmetrical coercivities. The value of H_{EB} peaks at $T << T_N$ and then decreases as the temperature rises. This agrees well with the standard equation $H_{EB} = -\frac{J}{M_S d_F}$ [44]. The austenite to martensite transformation starts at $T_{AMs} \approx 219$ K and finishes at $T_{AMf} \approx 40$ K, whereas the reverse martensitic transformation occurs at $T_{MAs} \approx 62$ K and finishes at $T_{MAf} \approx 248$ K. The metallic behaviour of the films changes to semiconducting nature with the lowering of temperature. It is interesting to note the occurrence of a weak reentrant metallic behaviour in the region exhibiting reentrant FM at T < 36 K (during cooling) and up to T ~ 62 K (during warming). The maximum MR values of ≈ 3.25% and ≈ 2.59% for H = 50 kOe in the present films are observed at 150 K and 240 K respectively, i.e. at $T < T_N$ region, where there is a delicate coexistence of AFM and FM phases.

Acknowledgements One of the authors (BB) would like to thank DST-INSPIRE for providing the INSPIRE fellowship. The authors would like to thank Dr. K. K. Maurya for the HRXRD and Dr. Kedar Singh (JNU) for R-T measurements. The authors are also thankful to Director, USIC-University of Rajasthan, Jaipur for the use of the SQUID magnetometer facility created under the UGC-UPE program 'Focused Area' for magnetization measurement. The authors would like to thank Mr. Sandeep Singh for the MFM characterizations.

Funding information Major equipment funding has been provided by the Council of Scientific and Industrial Research (CSIR).

References

1. Webster, P.J.: Heusler alloys. Contemp. Phys. **10**, 559 (1969)
2. Nanda, B.R.K., Dasgupta, I.: J. Phys. Condens. Matter. **15**, 7307 (2003)
3. Galanakis, I., Mavropoulos, P., Dederichs, P.H.: J. Phys. D. Appl. Phys. B. **765**, (2006)
4. Galanakis, I., Mavropoulos, P.: J. Phys. Condens. Matter. **19**, 315213 (2007)
5. Planes, A., Mañosa, L., Acet, M.: J. Phys. Condens. Matter. **21**, 233201 (2009)
6. Felser, C., Wollmann, L., Chadov, S., Fecher, G.H., Parkin, S.S.P.: APL Mater. **3**, 41518 (2015)
7. Bainsla, L., Suresh, K.G.: Citation Appl. Phys. Rev. **3**, 031101 (2016)
8. Sutou, Y., Imano, Y., Koeda, N., Omori, T., Kainuma, R., Ishida, K., Oikawa, K.: Appl. Phys. Lett. **85**, 4358 (2004)
9. Graf, T., Felser, C., Parkin, S.S.P.: Prog. Solid State Chem. **39**, 1 (2011)
10. Hernando, B., Sánchez Llamazares, J.L., Santos, J.D., Prida, V.M., Baldomir, D., Serantes, D., Varga, R., González, J.: Appl. Phys. Lett. **92**, 132507 (2008)
11. Aksoy, S., Acet, M., Deen, P.P., Mañosa, L., Planes, A.: Phys. Rev. B. **79**, 212401 (2009)
12. Chatterjee, S., Giri, S., De, S.K., Majumdar, S.: Phys. Rev. B. **79**, 92410 (2009)
13. Khan, M., Jung, J., Stoyko, S.S., Mar, A., Quetz, A., Samanta, T., Dubenko, I., Ali, N., Stadler, S., Chow, K.H.: Appl. Phys. Lett. **100**, 172403 (2012)
14. Tan, C.L., Huang, Y.W., Tian, X.H., Jiang, J.X., Cai, W.: Appl. Phys. Lett. **100**, 132402 (2012)
15. Zayak, A.T., Adeagbo, W.A., Entel, P., Rabe, K.M.: Appl. Phys. Lett. **88**, 2004 (2006)
16. Xuan, H.C., Cao, Q.Q., Zhang, C.L., Ma, S.C., Chen, S.Y., Wang, D.H., Du Appl, Y.W.: Phys. Lett. **96**, 202502 (2010)
17. Santos, J.D., Sanchez, T., Alvarez, P., Sanchez, M.L., Sánchez Llamazares, J.L., Hernando, B., Escoda, L., Suñol, J.J., Varga, R.: J. Appl. Phys. **103**, 07B326 (2008)
18. Zhang, Y., Zhang, L., Zheng, Q., Zheng, X., Li, M., Du, J., Yan, A.: Sci. Rep. **5**, 11010 (2015)
19. Singh, N., Borgohain, B., Srivastava, A.K., Dhar, A., Singh, H.K.: Appl. Phys. A Mater. Sci. Process. **122**, 237 (2016)
20. Auge, A., Teichert, N., Meinert, M., Reiss, G., Hütten, A., Yüzüak, E., Dincer, I., Elerman, Y., Ennen, I., Schattschneider, P.: Phys. Rev. B. **85**, 214118 (2012)
21. Dunand, D.C., Müllner, P.: Adv. Mater. **23**, 216 (2011)
22. Malygin, G.A.: Tech. Phys. **54**, 1782 (2009)
23. Roytburd, A.L., Kim, T.S., Su, Q., Slutsker, J., Wuttig, M.: Acta Mater. **46**, 5095 (1998)
24. Vishnoi, R., Singhal, R., Kaur, D.: J. Nanopart. Res. **13**, 3975 (2011)
25. Dubowik, J., Zał ski, K., Gościańska, I., Głowiński, H., Ehresmann, a.: Appl. Phys. Lett. **100**, 162403 (2012)
26. Behler, A., Teichert, N., Dutta, B., Waske, A., Hickel, T., Auge, A., Hütten, A., Eckert, J.: AIP Adv. **3**, 122112 (2013)
27. Pandey, S., Quetz, A., Aryal, A., Dubenko, I., Mazumdar, D., Stadler, S., Ali, N.: Magnetochemistry. **3**, 3 (2017)
28. Pandey, S., Us Saleheen, A., Quetz, A., Chen, J.-H., Aryal, A., Dubenko, I., Stadler, S., Ali, N.: AIP Adv. **8**, 56408 (2018)
29. Jing, C., Li, Z., Zhang, H.L., Chen, J.P., Qiao, Y.F., Cao, S.X., Zhang, J.C.: Eur. Phys. J. B. **67**, 193 (2009)
30. Han, Z.D., Wang, D.H., Zhang, C.L., Xuan, H.C., Zhang, J.R., Gu, B.X., Du, Y.W.: Mater. Sci. Eng. B. **157**, 40 (2009)
31. Castillo-Villa, P.O., Mañosa, L., Planes, A., Soto-Parra, D.E., Sánchez-Llamazares, J.L., Flores-Zúñiga, H., Frontera, C.: J. Appl. Phys. **113**, 53506 (2013)
32. Fukushima, K., Sano, K., Kanomata, T., Nishihara, H., Furutani, Y., Shishido, T., Ito, W., Umetsu, R.Y., Kainuma, R., Oikawa, K., Ishida, K.: Scr. Mater. **61**, 813 (2009)
33. Machavarapu, R., Jakob, G.: Appl. Phys. Lett. **102**, 232406 (2013)
34. Vishnoi, R., Kaur, D.: J. Alloys Compd. **509**, 2833 (2011)
35. Modak, R., Raja, M.M., Srinivasan, A.: J. Magn. Magn. Mater. **448**, 146 (2018)
36. Golub, V.O., Lvov, V.A., Aseguinolaza, I., Salyuk, O., Popadiuk, D., Kharlan, Y., Kakazei, G.N., Araujo, J.P., Barandiaran, J.M., Chernenko, V.A.: Phys. Rev. B. **95**(24422), (2017)
37. Krenke, T., Acet, M., Wassermann, E., Moya, X., Mañosa, L., Planes, A.: Phys. Rev. B. **72**, 14412 (2005)
38. Tao, Q., Han, Z.D., Wang, J.J., Qian, B., Zhang, P., Jiang, X.F., Wang, D.H., Du, Y.W.: AIP Adv. **2**, 042181 (2012)
39. Aydogdu, Y., et al.: J. Alloys Compd. **683**, 339 (2016)
40. Sokolovskiy, V.V., Buchelnikov, V.D., Zagrebin, M.A., Entel, P., Sahoo, S., Ogura, M.: Phys. Rev. B. **86**, 134418 (2012)
41. Kundu, A., Ghosh, S.: J. Phys.: Condens. Matter. **30**(015401), (2018)
42. Czaja, P., Chulist, R., Zywczak, A., Hawelek, L., Przewoznik, J.: Magnetochemistry. **3**, 24 (2017)
43. Borgohain, B., Siwach, P.K., Singh, N., Singh, H.K.: J. Magn. Magn. Mater. **454**, 13 (2018)
44. Getzlaff, M.: Fundamentals of Magnetism. Springer-Verlag Berlin, Heidelberg (2008)
45. Nayak, A.K., Shekhar, C., Winterlik, J., Gupta, A., Felser, C.: Appl. Phys. Lett. **100**, 152404 (2012)
46. Sharma, J., Suresh, K.G.: Appl. Phys. Lett. **106**, 072405 (2015)
47. Pal, D., Ghosh, K., Mandal, K.: J. Mag. Magnet. Mater. **360**, 183 (2014)
48. Du, Y., Xu, G.Z., Zhang, X.M., Liu, Z.Y., Yu, S.Y., Liu, E.K., Wang, W.H., Wu, G.H.: Europhys. Lett. **103**, 37011 (2013)
49. Sato, T., Kokado, S., Kosaka, S., Ishikawa, T., Ogawa, T., Tsunoda, M.: Appl. Phys. Lett. **113**, 112407 (2018)